THE JOURNAL OF PHYSICAL CHEMISTRY C
A JOURNAL OF THE AMERICAN CHEMICAL SOCIETY

pubs.acs.org/JPCC
Article

Interplay of Ionic and Electronic Properties of LPSCl with Its Micro- and Macrostructural Dynamics

Sara Pacetti, Christoffer Karlsson, Emin Mijit, Marcel Drüschler, Andrea Di Cicco, Nicola Pinto, Dominic Bresser, and Javad Rezvani*

Cite This: J. Phys. Chem. C 2026, 130, 3040−3049

ABSTRACT: A systematic study is performed to correlate the electronic and ionic properties of Li_6PS_5Cl (LPSCl) with its mechanical properties and structural dynamics as a function of pressure and temperature. The crucial role of mechanical and structural dynamics, from the atomic to the macroscale, is investigated to optimize electrolyte properties and assembly. Ionic conduction dynamics are described via particle rearrangement, plastic deformation, contact formation, and activation volume with respect to structural dynamics during compression and decompression. The results demonstrate the potential for optimizing electrolyte performance through the interplay of opportune pelletizing and stacking pressures. High pelletizing pressures enhance ionic conductivity and electrical contact uniformity, whereas pressures below 80 MPa introduce interface contact instabilities. Additionally, it is shown that applying high pressure (above 10 GPa) results in irreversible structural modifications. At pelletizing pressures, ionic conductivity is dominated by grain boundaries; at stacking pressures, however, they contribute equally to the grain bulk. As a result of positive activation volume, ionic conductivity peaks at a stack pressure of 80 MPa, after pelletizing at a higher pressure. Defects can introduce donor levels into the energy gap of LPSCl, which can be adjusted to improve battery performance.

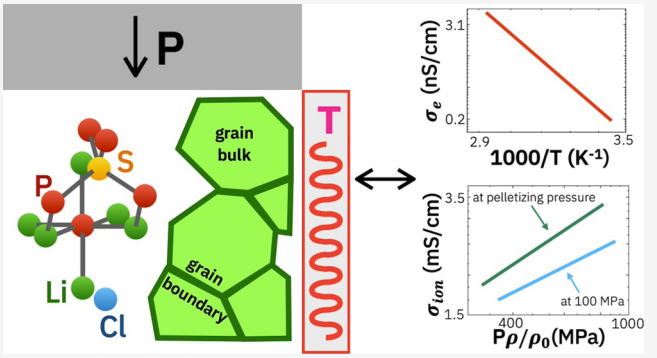

INTRODUCTION

All-solid-state Li batteries promise higher energy densities along with enhanced safety compared to liquid organic electrolytes.[1−4] However, their lower ionic conductivity at ambient temperature and their high reactivity at very low and high potentials still hinder their widespread commercial application.[5−7] Compared to liquid electrolytes, they also present a higher contact resistance, which limits a facile charge transfer at the electrode−electrolyte interface, in particular at low stack pressures.[8] Solid electrolytes are not completely free from short-circuiting either, which is common when combined with lithium−metal electrodes due to lithium dendrites. Solid electrolytes introduce asperity and imperfections at the interfaces[9]; as a consequence, the electronic current is more localized, and Li dendrite growth is enhanced.[10] Hence, in order to ameliorate the ionic conductivity while reducing the electronic conductivity, thermal and/or mechanical treatments are employed.[11]

Solid sulfide electrolytes have been reported to be promising candidates for extensive applications in all-solid-state batteries, although they suffer from instability under air exposure.[12] This material class exhibits a particularly high ionic conductivity of up to 2 mS cm^{-1} that surpasses even that of conventional organic liquid electrolytes. This is accompanied by a ductile nature,[6] which makes them easily processable and able to form good contacts with the electrodes, even at low processing temperatures.[7] In this way, surface imperfections and the consequent contact resistance can be reduced.[13] Argyrodite-type sulfidic solid electrolytes are among the most well-known materials in this class and are widely used in the fabrication of all-solid-state batteries. Their general formula is Li_6PS_5X (X = Cl, Br, I) with X^- anions forming a face-centered cubic (fcc) lattice, while S^{2-} ions and PS_4^{3-} units occupy the tetrahedral and octahedral sites, respectively.[6] In particular, the Li_6PS_5X structure shows an enhanced lithium transport[14] due to its anion disorder and Li interstitial/vacancies, which reduce the activation energy for Li^+-ion diffusion by modification of the Li-ion site energies.[6]

The degree of compaction and proper contact at the interfaces depend on the applied pressure during fabrication, and they crucially influence the battery operation and the

Received: September 5, 2025
Revised: January 13, 2026
Accepted: January 14, 2026
Published: February 12, 2026

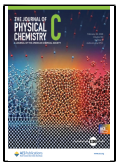

https://doi.org/10.1021/acs.jpcc.5c06227
J. Phys. Chem. C 2026, 130, 3040−3049

electronic/ionic properties of the solid electrolyte. Reducing the porosity can increase the particle−particle contact and reduce the conduction path tortuosity, therefore increasing the ionic conductivity while decreasing the contact resistance. Also, grain boundaries can affect ionic conduction, as they introduce resistance to ionic migration; however, this effect can be minimized by applying pressure.[15,16]

Recent studies on argyrodite electrolytes have emphasized their potential from an ionic/electronic conduction point of view. However, a systematic study correlating micro- and macrostructural dynamics with electronic, ionic, and mechanical properties is lacking. Furthermore, despite the role of the electronic current in battery self-discharge and short-circuiting, the electron conduction mechanism and its temperature dependence have not yet been extensively investigated. This information is crucial for optimizing the properties of the electrolyte based on preparation pressure (pelletizing) and synthesis.

This work examines the correlation between the micro/macrostructural modifications of Li_6PS_5Cl (LPSCl) and its ionic and electronic properties, with the aim of optimizing the synthesis and working conditions. The material's specific properties were investigated using several microscopic and spectroscopic techniques (e.g., scanning electron microscopy (SEM), Raman spectroscopy, electrochemical impedance spectroscopy, and DC resistance measurement) and as a function of temperature and pressure. The effects of pelletizing and stacking pressures, as well as the contributions of grain bulk and boundaries to ionic conductivity, were also examined. Finally, the electronic conduction mechanism and its temperature dependence are discussed in the context of structural disorder, creating impurity levels in the dielectric gap of LPSCl.

RESULTS AND DISCUSSION

Pristine Sample

The morphology of the pristine LPSCl sample was investigated by using SEM on the uncompressed powder sample (see Figure 1a,b). The results show a porous structure with interconnected particles. Their size and pore width were estimated to be about 5−6 and 0.6−5.4 μm, respectively. The energy-dispersive spectroscopy (EDS) analysis was performed in order to investigate the stoichiometry and purity of the sample, which shows a uniform element distribution without ionic impurities in the investigated powder (see Figure 1c, details in the Supporting Information).

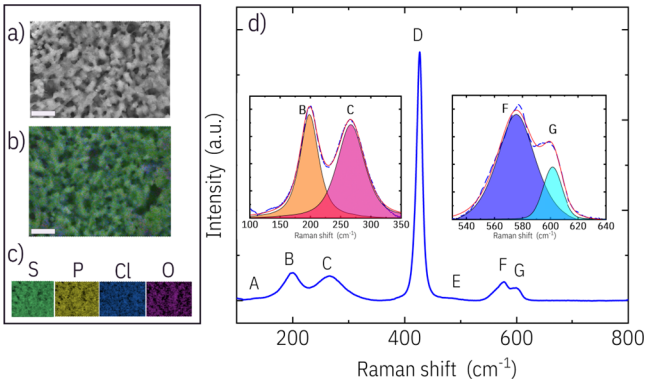

Figure 1. (a) SEM images of the pristine LPSCl electrolyte along with (b) the EDS map. The scale bars are 10 μm. (c) Individual EDS maps of the elements. (d) Raman spectra of the LPSCl powder along with the least-squares fitting.

The structure of the uncompressed LPSCl was then assessed by Raman spectroscopy from the powder at ambient pressure (see Figure 1d). The five main peaks can be distinguished at 198, 267, 426, 576, and 602 cm^{-1} and are assigned to the vibrational modes of the thiophosphate group PS_4^{3-}. These correspond to ν_1, ν_2, ν_3, and ν_4 vibrational modes, which correspond to symmetric P−S stretching[17−20] (D band), symmetric bending of PS_4^{3-}[17−20] (B band), asymmetric stretching of PS_4^{3-}[18,20,21] (F and G bands), and asymmetric bending of S−P−S in PS_4^{3-}[19,22] (C band), respectively (Table 1). These features were fitted with pseudo-Voigt curves, and

Table 1. Raman Spectroscopy Peak of LPSCl

	ν (cm^{-1})	FWHM (cm^{-1})	vibrational mode (cm^{-1})	references
A	∼145		S−S−S bending	17,23
B	198.4(1)	37.1(4)	ν_2 (PS_4^{3-})	17,19
C	266.8(2)	54.1(5)	ν_4 (PS_4^{3-})	19,22
D	426.33(4)	12.5(1)	ν_1 (PS_4^{3-})	17−20
E	∼481		S−S stretching	23,24
F	575.5(2)	33.4(6)	ν_3 (PS_4^{3-})	18,20,21
G	601.5(3)	16.1(6)	ν_3 (PS_4^{3-})	18,20,21

the results showed no evidence of ionic intermixing. Two hardly distinguishable bands were also observed at about 145 and 481 cm^{-1}, which are tentatively assigned to the vibrations of S−S−S bending[17,23] and S−S stretching[23,24] and can be associated with the impurities of Li_2S_x and P_2S_x, resulting from the synthesis procedure.[23,25−31] This indicates the possible presence of the initial precursor phases within the pristine powder.

Macrostructure Properties

In order to increase contact between particles and thus enhance the ionic conductivity, solid electrolytes need to be compressed prior to use. Based on the applied pressure, the powder can evolve through three different regimes: (I) the particles rearrange in a way that the smaller ones fill the voids between the larger ones, as well as the voids between particles and walls; (II) local stresses exceed the elastic limit of the single particles and the consolidation occurs, driven by fragmentation. This especially occurs in more brittle materials or by plastic deformation in softer materials; (III) the sample is heavily densified, and individual particles are no longer distinguishable. In this case, the pellet behaves like a single body that can be elastically deformed.[8,32,33] The relation between the porosity, density, and pressure can be expressed via the Heckel equation[34]:

$$-\ln(\epsilon) = KP + A \quad (1)$$

where porosity is $\epsilon = 1 - \rho/\rho_0$, with ρ the sample density at pelletizing pressure P and ρ_0 being the density at full compaction, i.e., the bulk density. The density was estimated from the XRD results (Figure S2a) to be around 1.629 g/cm^3. K is the slope of the linear region in the Heckel plot, which displays the $\ln(\epsilon)$ against pelletizing pressure, and A, which results from the $\ln(\epsilon)$ at zero pressure, depends on the initial particle rearrangement.[34] In the case of 'out-of-die' measurements, the reciprocal of K is called the mean yield pressure P_y. For 'in-die' measurements, it is called the apparent mean yield pressure P'_y. The mean yield pressure describes a material's

https://doi.org/10.1021/acs.jpcc.5c06227
J. Phys. Chem. C 2026, 130, 3040−3049

ability to undergo plastic deformation.[32] Figure 2 displays the Heckel plot for LPSCl, showing -ln(ϵ) as a function of the

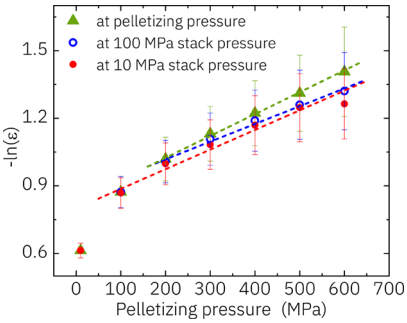

Figure 2. Heckel plot obtained for data at pelletizing pressure, at 100 MPa stack pressure, and at 10 MPa stack pressure; these three data sets are plotted as a function of pelletizing pressure. The dashed lines emphasize the linear regions.

pelletizing pressure. The measurements show an initial nonlinear increase, followed by a linearly increasing region starting from around 100−200 MPa. The initial nonlinear region detected in the "in-die" curve indicates the rearrangement of particles in order to fill the empty voids (the dominance of regime I). From around 200 MPa onward, particle deformation commences and results in the domination of regime II. This linear region persists up to 600 MPa; this indicates that a full densification of the sample (regime III) is never reached. The mean yield pressure, P_y (measured at pelletizing pressure), and the apparent mean yield pressure, P'_y (measured at 10 MPa), were estimated in the linear region of the Heckel plot, resulting in P_y to be 1100 ± 100 MPa between 100 and 600 MPa, and P'_y to be 1020 ± 30 MPa between 200 and 600 MPa. The small difference observed between P_y and P'_y indicates a negligible contribution of elastic deformations in this pressure range.

Microstructural Dynamics

In order to investigate the correlation between the pressure-dependent ionic transport and the structural dynamics, in situ Raman spectroscopy was employed under a cycle of compression and decompression up to around 20 GPa (see Figure 3). In order to keep the samples tightly sealed to avoid any air exposure, the measurements were performed at pressures higher than ∼600 MPa. The results show the induction of structural stress via a blue shift of peak centers, already visible upon compression at 800 MPa (see Figure 3). The lattice distortion persists up to about 10 GPa, at which the sample undergoes amorphization, according to the sudden increase of the full width at half-maximum (FWHM) of the D peak (see Figure 3a). These results are in agreement with the XRD results reported by Faka et al.,[35] where the peak broadening at high pressure and the background increase at lower q suggest a greater disorder in the system. Further amorphization was observed via broadening of the Raman features up to 20 GPa. Band A intensifies during the compression, and the intensity of peaks B and C gradually interchanges; meanwhile, peaks F and G maintain their ratio during the pressure application cycle. The increase in the asymmetric bending of the PS_4 structure (feature C) indicates the distortion of the P−S atomic distance in the base of the tetrahedra. This results in an increased S−S−S bending and

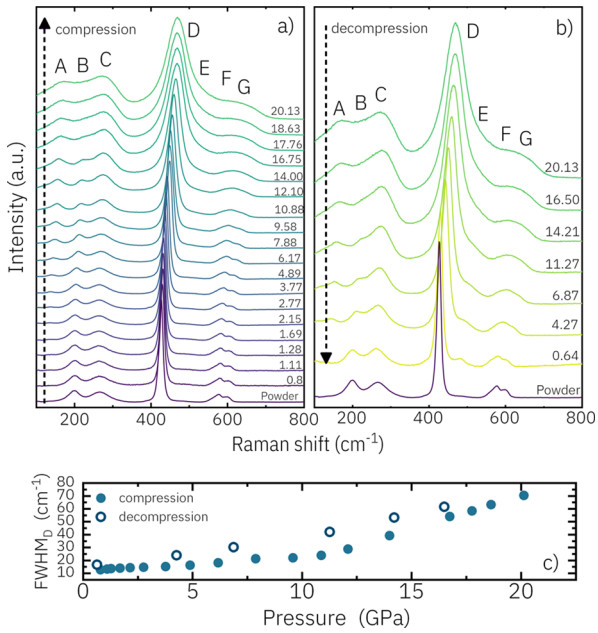

Figure 3. Raman spectra of LPSCl powder in the DAC anvil cell, separated for (a) increasing pressure and (b) decreasing pressure. Numeric labels are pressures expressed in the GPa. Changes in peak positions and FWHM are clearly visible. The spectrum of the pristine uncompressed powder is also plotted in both figures as reference. (c) FWHM of Raman D band derived by fitting is plotted as a function of the applied pressure during both compression and decompression.

the enhancement of the A band. The S−S−S bending is a characteristic feature of lithium polysulfides[23,25] and phosphorus sulfides.[26−31] These results suggest either an increase in the coordination number of central P to S ligands, without a phase transition, or an increase in the formation of other polysulfides. Upon decompression, a slower recrystallization was detected (see Figure 3b) with relative reversibility of the phase structure. The resulting spectra show the disappearance of the A band, while the E band persists. Our findings suggest that the atomic structural modification, particularly below 1 GPa, which is used for conductivity measurements, is limited to lattice distortion, with no ionic intermixing or formation of metastable phases. However, further complementary experiments, such as in situ X-ray diffraction measurements, are also required to confirm the origin of modifications after the full compression and decompression cycle.

Ionic and Electronic Conductivity

The electrochemical properties of solid electrolytes can be investigated using EIS in a nondestructive way. This allows the electrochemical processes involved to be examined and the ionic conductivity of the electrolyte and the resistance of the grain bulk and boundaries to be derived.[36] The electronic conductivity, on the other hand, can be derived by application of DC polarization via two ion-blocking electrodes. Following the application of a DC potential, a constant current is expected in the steady state, with the only contribution to the current coming from electronic carriers.[37]

The pressure dependence of the system conductivity was investigated between 10 and 650 MPa due to the absence of a chemical phase transition in this pressure range, confirmed via microstructural dynamics investigation. A lower threshold of 10 MPa was chosen for electrical measurements since, below this value, the contact between the ion-blocking electrode and

https://doi.org/10.1021/acs.jpcc.5c06227
J. Phys. Chem. C 2026, 130, 3040−3049

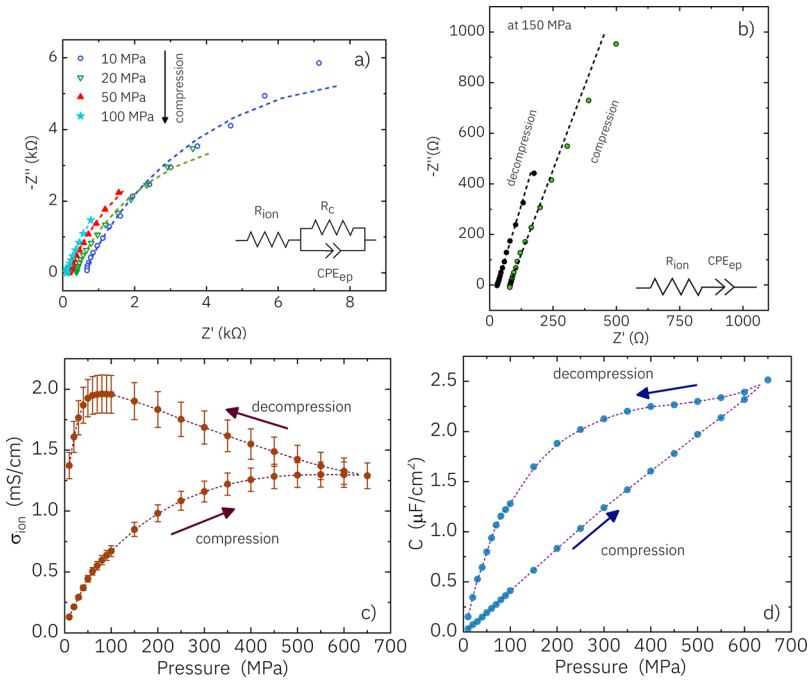

Figure 4. Nyquist plots of LPSCl (a) at fixed pressures ranging from 10 to 100 MPa, measured between 100 Hz and 700 kHz, and (b) at 150 MPa before and after pelletizing at 650 MPa, measured between 100 Hz and 1 MHz. Broken lines are least-squares fitting by the ECMs depicted inside each graph. Pressure-dependent (c) conductivity, σ_{ion}, and (d) equivalent capacitance C, at a constant temperature of 25 °C, are extracted by the fitting process. Arrows indicate in which order the points were recorded.

the electrolyte is insufficient for reliable measurement. The impedance spectra at 25 °C up to 100 MPa (see Figure 4a) could be fitted with an ionic resistance in series with a constant phase element, with a parallel contact resistance (i.e., $R_{ion} - (R_c)(\mathrm{CPE}_{ep})$ circuit), where R_{ion} refers to the sample ionic resistance. The constant phase element CPE_{ep} refers to the double-layer polarization at the electrolyte/electrode interface,[38−40] and the resistance R_c refers to an additional contact resistance between the electrolyte and electrode.[13,41,42] This resistance is eliminated at pressures above ∼100 MPa due to the contact improvement via the electrolyte compaction. From ∼150 MPa, the more uniform contact between the electrode and electrolyte allows us to fit the impedance via a $R_{ion} - \mathrm{CPE}_{ep}$ series circuit (see Figure 4b), which persists up to 650 MPa. A clear distinction between grain bulk and grain boundary conductivities is hindered by the absence of their representative semicircles in the EIS spectra, as a consequence of a small charge polarization at the grain boundaries. Therefore, only the polarization capacitance at the interface with the electrode (C) and the overall ionic conductivity of the system (σ_i) could be estimated for the compression/decompression cycle. The capacitance C was estimated from Brug's formula

$$C = \left(\frac{Q}{R^{\alpha-1}}\right)^{1/\alpha} \tag{2}$$

where Q and α describe the constant phase element impedance $Z_{\mathrm{CPE}} = Q(i\omega)^{-\alpha}$, with i being the imaginary unit and ω being the frequency of the AC signal applied. The ionic conductivity was derived from the pellet thickness, d, resistance R_i, and cross-sectional area A:

$$\sigma_i = \frac{d}{R_i A} \tag{3}$$

Our results show that the capacitance and ionic conductivity both increase with increasing pressure (Figure 4c,d). The capacity increase in the compression regime is in agreement with the enhanced contact at the electrode−electrolyte interface due to plastic deformation of the particles,[13] which increases the surface-to-distance ratio. In the decompression regime, C decreases gradually, with a faster rate of decrease particularly below 100 MPa before returning to its initial value. The higher capacity value during decompression versus compression confirms the plastic deformation of the particles. The σ_i rapid increase in compression regime up to 100 MPa is also in agreement with the contact formation process between the electrode and electrolyte, as well as the consolidation process, which reduces tortuosity for Li-ion diffusion pathways. At higher compression pressures, σ_i stabilizes and reaches a plateau at around 500 MPa. During decompression, σ_i first rises, attaining a maximum at 80 MPa and then rapidly drops. At the lowest applied pressure, σ_i does not recover the initial value due to the increase in the contact resistance and particle consolidation. The decrease in σ_i during the decompression sweep is the consequence of contact resistance at the electrode interface. The higher σ_i during the decompression sweep is a result of the elastic distortion of the crystal lattice and LPSCl-positive activation volume. The activation volume (V_a) is a local change in the atomic structure of the material and is associated with ion migration. It can be considered as the difference between the molar volume required for ion migration (V_m) and the molar free volume already available in the structure (V_f).[43] It ranges from negative to positive values depending on whether the lattice needs to shrink or expand to allow the ion migration.[8] By assuming a pressure-independent prefactor in the Arrhenius equation for ionic conduction (see eq 7),[44] the crystal distortion could be

https://doi.org/10.1021/acs.jpcc.5c06227
J. Phys. Chem. C 2026, 130, 3040−3049

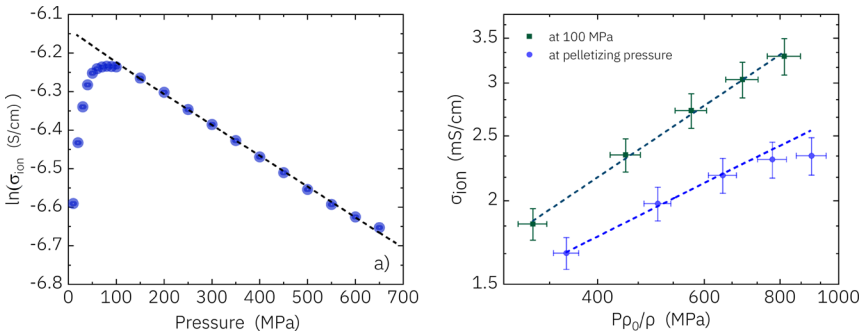

Figure 5. (a) $\ln(\sigma_i)$ as a function of pressure, collected during decompression. The activation volume was derived from a linear least-squares fitting (dashed line) of the linear region. (b) Least squares fitting (dashed lines) of the linear region of $\log(\sigma_i)$ against $\log(P\rho_0/\rho)$ (points).

examined from the relation between $\ln(\sigma_i)$ and pressure at a constant temperature (T)[1,8]

$$V_a \approx -k_B T\left(\frac{\partial \ln(\sigma_i)}{\partial P}\right)_T \tag{4}$$

where k_B is the Boltzmann constant and P is the applied pressure. When the pressure applied to the pristine powder increases, consolidation effects introduce deviations of $\ln(\sigma)$ from linearity. Therefore, V_a was estimated on the decreasing pressure sweep.[8] In the linear region, above 150 MPa (Figure 5a), the activation volume was calculated to be 1.98 ± 0.02 cm^3/mol. This result is in agreement with reported activation volumes for Li^+-ion-conducting solid electrolytes, as suggested based on the correlation between the activation volume and S/Cl anion disorder percentage.[8,45]

Besides the overall ionic conductivity, the grain bulk and grain boundary conductivity are key factors in ionic conduction. In most cases, grain boundaries are a limiting factor[46,47]; however, in some electrolytes, they conduct better than the bulk[48] since ionic conduction can occur not only between adjacent grains but also on their surface within the boundaries. The estimation of this kind of conductivity is not always straightforward due to the absence of the semicircle in the EIS spectrum related to grain boundary polarization.[49,50] Nonetheless, a tentative way to derive the grain boundary and bulk contributions to conductivity from pressure-dependent global conductivity of solid electrolytes has been suggested by Yamakov et al.[51] This theoretical model describes the whole polycrystalline electrolyte as a system of particles, taking into account their mechanical properties, and the compression at the contact point between particles and at the electrode surface. Similarly, the ionic conductivity is described by a network of resistances, each characterized by a combination of bulk and grain boundary resistances correlated with the contact surface and volume per particle. The total ionic conductivity is related to pressure by

$$\sigma_i \sim \left(P\frac{\rho_0}{\rho}\right)^{\eta} \tag{5}$$

where $P\frac{\rho_0}{\rho}$ will be referred to as rescaled pelletizing pressure and ρ was recorded at the same pressure of σ_i measurement, as described in the pressure ramp of Figure 7c. η is a characteristic exponent, which changes according to the packing of the system (e.g., hexagonal close packing, HCP, and randomly packed, RND) and domination of the grain bulk (σ_B) or grain boundary (σ_{GB}) conductivity as follows:

$$\sigma_B \gg \sigma_{GB}\text{: } \eta_{HCP} \approx 2/3,\ \eta_{RND} \approx 3/4$$
$$\sigma_B \ll \sigma_{GB}\text{: } \eta_{HCP} \approx 1/3,\ \eta_{RND} \approx 1/2 \tag{6}$$

These relations can be used to derive the particle packing and dominating ionic conductivity from the value of η. This simplified model is only a function of the contact area between grains and does not consider the mechanical properties, particle size, or the morphology of the electrolyte, all of which can play important roles for the ionic conductivity. As a consequence, the data "at pelletizing pressure" are expected to deviate from the data "at 100 MPa stack pressure". At pelletizing pressures above ~500 MPa, the "in-die" conductivity deviates from linearity due to the lattice distortion at high pressures, in agreement with Raman spectroscopy results. Hence, the data at the higher pelletizing pressure cannot be explained by the model. The change in the slope of σ_i against rescaled pelletizing pressure was fitted in the linear ranges (Figure 5b), corresponding to η values of 0.46 ± 0.03 and 0.62 ± 0.02 at pelletizing pressure and at 100 MPa stack pressure, respectively. As there will always be some disorder in the packing of LPSCl grains, the values of η are interpreted according to RND packing. The data "at pelletizing pressure" correspond to $\sigma_B \ll \sigma_{GB}$, while the η at 100 MPa stack pressure falls in between the values for $\sigma_B \ll \sigma_{GB}$ and $\sigma_{GB} \ll \sigma_B$. This analysis shows that, at high pelletizing pressures, ionic conductivity is dominated by grain boundaries. However, releasing the pressure to 100 MPa results in an equilibrium between the ionic conductivities of the grain bulk and boundaries. The grain boundary conductivity domination, a consequence of the higher applied pressure,[51,52] is a result of an increase in the particle compactness and the decrease of the interfacial energy barrier for ion migration within grain boundaries.[15]

The ionic and electronic conduction were also studied as a function of the temperature in order to investigate thermally activated mechanisms valid for both conduction processes. The experimental setup was used in the conventional operating temperature range (about 20−70 °C) and at a pressure of ~200 MPa, which ensures complete particle rearrangement and good electrode/electrolyte contact. Li^+ ion conduction is a thermally activated process, consisting of ions migrating inside a crystal structure, and is described by the Arrhenius equation[1,8]:

$$\sigma_i = \sigma_0 e^{-E_a/k_B T} \tag{7}$$

where E_a is the activation energy and k_B is the Boltzmann constant. The E_a can be interpreted as the energy barrier

https://doi.org/10.1021/acs.jpcc.5c06227
J. Phys. Chem. C 2026, 130, 3040−3049

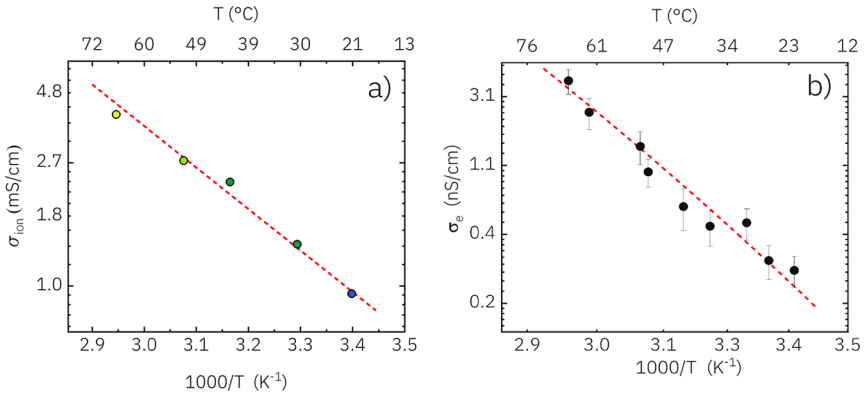

Figure 6. Arrhenius plot of ionic and electronic conductivity fitted by a linear least-squares fitting. Measurements were carried out at 200 MPa.

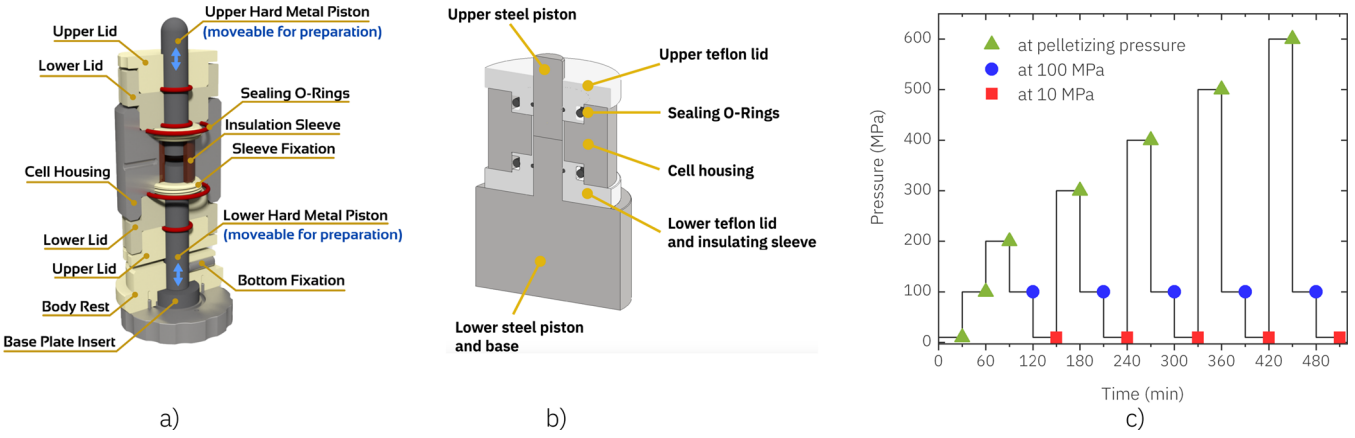

Figure 7. Cross section of the cells employed: (a) CompreCell 12-DP (rhd instruments GmbH & Co. KG): steel parts are shown in light gray, tungsten carbide parts are shown in dark gray, PEEK corresponds to yellow and brown; (b) homemade cell: gray parts are made of steel, and white parts are Teflon. O-rings are depicted in black. (c) The line describes the stepwise applied pressure, and the points indicate when density and conductivity were measured.

separating two points in the most energetically favorable pathway for Li^+ ion migration.[53] The sites involved and their energies are determined by the atomic bonding environment. σ_0 is a prefactor associated with the hopping length and frequency of Li^+ ion jumps from one lattice site to another.[1] The ionic conductivity was derived from the impedance spectra at different temperatures via an $R_{ion} - CPE_{eq}$ equivalent circuit. Fitting the data to the Arrhenius equation (6) resulted in an activation energy E_a = 0.30 ± 0.02 eV between 21 and 63 °C, in agreement with previous theoretical and experimental values, reported for LPSCl.[54,55] A comparison with the theoretically calculated relation between the S/Cl anion disorder and the ionic activation energy in LPSCl indicates an anion disorder lower than 30% in our system in this temperature range. This is a detrimental effect for battery performance since an optimal S/Cl anion disorder can improve ionic conduction and tune the activation volume.[6,45,56]

The electronic conduction also follows the Arrhenius equation ($\sigma_e = \sigma_0 e^{-E_a/k_B T}$), with an electronic activation energy E_a = 0.54 ± 0.04 eV from the Arrhenius plot (see Figure 6b). The activation energy is a well-known method to estimate possible levels close to the conduction/valence band. Since the band gap of LPSCl is between 2.14 and 4.86 eV, the lower activation energy for the electronic conduction can be attributed to the energy levels within the gap.[57−59] This effect has also been detected in LPSCl by Gorai et al.,[59] who correlated these levels to the presence of defects, mainly lithium interstitial and sulfur/chloride antisites. It is suggested that the presence of disorders introduces donor-like levels of excess free electrons into the gap of LPSCl, which could explain the obtained activation energy.[59−62]

EXPERIMENTAL SECTION

LPSCl powder under study was sourced from MSE Supplies under the commercial brand name Ampcera, synthesized from >99.9% precursor materials. The declared mass median diameter of the particles is 1 μm, as selected by a 325 mesh sieve. LPSCl is typically prepared by a solid-state sintering method: a stoichiometric mixture of Li_2S, P_2S_5, and LiCl is mixed by ball-milling at about 600 rpm for 10−20 h and successively heated at 550 °C for 5 h in an Ar atmosphere.[54,63−65] The morphology was analyzed by SEM and optical microscopy. In order to transfer the sample into the SEM chamber, it was shortly exposed to air. EDS was also carried out within the SEM chamber.

Raman spectroscopy was performed with a 532 nm wavelength laser. For Raman measurements at ambient pressure, the sample was sealed in an argon atmosphere inside specifically designed airtight cells (see Figure S1 in the Supporting Information). For in situ Raman experiments, a Le Toullec-type membrane-driven diamond anvil cell[66] was used. The sample was loaded and sealed in a N_2 glove bag to avoid exposure to air. Prior to sample loading, small ruby spheres were placed in the empty gasket and dried in an oven for about 1 h at 100 °C, together with the entire cell assembly, to remove humidity. No pressure-transmitting medium was added in order to avoid any reaction with the sample. The pressure and spectra were measured using a micro laser beam (~2 μm); hence, they could be reliably measured in the vicinity of the ruby sphere by the standard

https://doi.org/10.1021/acs.jpcc.5c06227
J. Phys. Chem. C 2026, 130, 3040−3049

ruby fluorescence technique.[67] The target pressure was identified via the Raman shift of the Ruby crystal loaded alongside the sample in the cell. Five minutes equilibration time was applied before each measurement. The minimum pressure reached was 0.6 GPa in order to maintain the sealing of the samples from exposure to air.

Two different setups were employed in order to measure the temperature and pressure dependences of the ionic and electronic properties (see Figure 7a,b). One setup consisted of a CompreCell 12-DP measurement cell (rhd instruments GmbH & Co. KG) coupled with a CompreDrive (rhd instruments GmbH & Co. KG), a heating/cooling jacket coupled with a Presto A40 (Julabo GmbH) or Huber Unistat 405 (Peter Huber Kältemaschinenbau AG) circulator, and a Pt-100 temperature sensor, employed to keep the sample temperature constant. The sample was contacted by two φ = 12 mm tungsten carbide pistons in a polyether ether ketone (PEEK) sleeve. The changes in the sample thickness were monitored following the procedure described in ref 68 and considering an error on the motor position of ± 8.5 μm. With this setup, the pressure was applied stepwise, and 30 minutes waiting time was applied at each step to allow the system to equilibrate before recording the electrochemical impedance spectrum. The second cell was a homemade stainless steel cell (referred to in the next as a homemade cell) coupled with a 25 ton Graseby Specac hydraulic press, two heating strips coupled with a GW Instek (model GPR-6030D) power supply, and an uncompensated K-type thermocouple connected to a Fluke 52 K/J thermometer. With this setup, the sample was contacted by two φ = 8 mm steel pistons inside a Teflon sleeve. In this case, the pressure was adjusted to 200 MPa before recording each impedance spectrum, and approximately 1 minute waiting time was applied before recording each resistance value under DC polarization.

EIS spectra were recorded by applying a sinusoidal signal (AC) with a 10 mV amplitude and at fixed frequencies between 100 Hz and 1 MHz. DC resistance measurements were performed by applying a DC polarization of 400 mV (within the stability window). All the cells were assembled under an argon atmosphere. In particular, the CompreCell was kept overnight in a vacuum oven at 55 °C before assembling. The homemade cell was left overnight in a glovebox antechamber, under dynamic vacuum. The thickness change of the sample was taken into account in the ionic conductivity calculation only when not negligible, that is, only for the pressure-dependent measurements. The sample density, the grain bulk, and the grain boundary contributions to conductivity were acquired using a systematic pressure application measurement at specific points: "at pelletizing pressure," "at 100 MPa stack pressure," and "at 10 MPa stack pressure" (see Figure 7c), corresponding to sample "in-die" properties, optimal operating conditions, and sample "out-of-die" properties, respectively.

CONCLUSIONS

In the present work, the electronic and ionic properties of the LPSCl electrolyte were investigated based on its macro- and microstructural properties and dynamics as a function of temperature and pressure. The results show that the pre-application of pressure within electrode synthesis will start the ionic conduction modulation via particle rearrangements, followed by the plastic deformation at around 150 MPa. This rearrangement is also accompanied by enhanced contact formation at the interface. The lattice distortion due to crystal stress is confirmed via Raman spectroscopy. Irreversible structural changes (possible side products and decompositions), as well as amorphization above 10 GPa, were revealed by in situ Raman spectroscopy. Pelletizing pressure of 650 MPa shows an optimal compaction, inducing a higher ionic conduction, due to the enhanced particle−particle and grain contacts. This also induces a more uniform interface contact that can be maintained upon decompression. The ionic conductivity of LPSCl has shown to be dominated by the grain boundary conduction at high pelletizing pressures, while at lower stacking pressure, the bulk conduction becomes comparable to that of grain boundaries and the conduction is increased due to the positive activation volume. Furthermore, the plastic and elastic deformation of the particles and crystallites, respectively, will reach an equilibrium at the high pelletizing pressure that results in a relatively constant ionic conduction. The electronic conductivity suggests the presence of defects (e.g., antisites and Li interstitials) via introducing deep electronic levels into the gap of LPSCl, with a lower activation energy compared to that of the material gap. Our results suggest the possibility of tuning and optimization of the required parameters, such as the ionic and electronic properties, for predesigned device fabrications. High pressures are recommended to guarantee proper electrical contact, particle−particle adhesion, and a lower energy barrier at the grain boundaries. At the same time, high pressures can induce significant lattice distortions, which are detrimental to ionic conduction. Further studies on the structural relaxation after long decompression, on the activation energy prefactor estimation, and on electronic transport in Hebb−Wagner geometry at working temperature seem appropriate. Further investigation into tailoring the optimal anion disorder in relation to the pelletizing pressure and working temperature, as well as phase transitions in the material at these temperatures and pressures, also seems necessary.

ASSOCIATED CONTENT

Supporting Information

The Supporting Information is available free of charge at https://pubs.acs.org/doi/10.1021/acs.jpcc.5c06227.

Photographs of Raman experimental setup, LPSCl XRD, pressure dependence of its density and Raman A and E bands, and temperature dependence of EIS spectra at 200 MPa (PDF)

AUTHOR INFORMATION

Corresponding Author

Javad Rezvani − *Physics Division, School of Science and Technology, University of Camerino, Camerino 62032, Italy;* orcid.org/0000-0002-6771-170X; Email: sj.rezvani@unicam.it

Authors

Sara Pacetti − *Physics Division, School of Science and Technology, University of Camerino, Camerino 62032, Italy*

Christoffer Karlsson − *rhd instruments GmbH & Co. KG, Darmstadt 64293, Germany*

Emin Mijit − *European Synchrotron Radiation Facility, Grenoble Cedex 9 38043, France; Sorbonne Université, Muséum National d'Histoire Naturelle, UMR CNRS 7590, Institut de Minéralogie, de Physique des Matériaux et de Cosmochimie, Paris 75005, France*

Marcel Drüschler − *rhd instruments GmbH & Co. KG, Darmstadt 64293, Germany*

Andrea Di Cicco − *Physics Division, School of Science and Technology, University of Camerino, Camerino 62032, Italy*

Nicola Pinto − *Physics Division, School of Science and Technology, University of Camerino, Camerino 62032, Italy*

Dominic Bresser − *Helmholtz Institute Ulm (HIU), Ulm 89081, Germany; Karlsruhe Institute of Technology (KIT),*

Karlsruhe 76021, Germany; Ulm University (UUlm), Ulm 89069, Germany; orcid.org/0000-0001-6429-6048

Complete contact information is available at: https://pubs.acs.org/10.1021/acs.jpcc.5c06227

Notes

The authors declare no competing financial interest.

■ ACKNOWLEDGMENTS

This work has been partially carried out within the project REFA (Grant Nos. 03EI6055 and 03EE6055A), funded by the Federal Ministry of Economic Affairs and Climate Action as part of the 7. Energieforschungsprogramm.

■ REFERENCES

(1) Famprikis, T.; Canepa, P.; Dawson, J. A.; Islam, M. S.; Masquelier, C. Fundamentals of inorganic solid-state electrolytes for batteries. *Nature materials* **2019**, *18*, 1278−1291.

(2) Chen, R.; Li, Q.; Yu, X.; Chen, L.; Li, H. Approaching practically accessible solid-state batteries: stability issues related to solid electrolytes and interfaces. *Chem. Rev.* **2020**, *120*, 6820−6877.

(3) Yu, C.; Ganapathy, S.; van Eck, E. R.; Wang, H.; Basak, S.; Li, Z.; Wagemaker, M. Accessing the bottleneck in all-solid state batteries, lithium-ion transport over the solid-electrolyte-electrode interface. *Nat. Commun.* **2017**, *8*, 1086.

(4) Ramakumar, S.; Deviannapoorani, C.; Dhivya, L.; Shankar, L. S.; Murugan, R. Lithium garnets: Synthesis, structure, Li^+ conductivity, Li^+ dynamics and applications. *Prog. Mater. Sci.* **2017**, *88*, 325−411.

(5) Boaretto, N.; Garbayo, I.; Valiyaveettil-SobhanRaj, S.; Quintela, A.; Li, C.; Casas-Cabanas, M.; Aguesse, F. Lithium solid-state batteries: State-of-the-art and challenges for materials, interfaces and processing. *J. Power Sources* **2021**, *502*, No. 229919.

(6) Zhou, L.; Minafra, N.; Zeier, W. G.; Nazar, L. F. Innovative approaches to Li-argyrodite solid electrolytes for all-solid-state lithium batteries. *Accounts of chemical research* **2021**, *54*, 2717−2728.

(7) Papakyriakou, M.; Lu, M.; Liu, Y.; Liu, Z.; Chen, H.; McDowell, M. T.; Xia, S. Mechanical behavior of inorganic lithium-conducting solid electrolytes. *J. Power Sources* **2021**, *516*, No. 230672.

(8) Schneider, C.; Schmidt, C. P.; Neumann, A.; Clausnitzer, M.; Sadowski, M.; Harm, S.; Meier, C.; Danner, T.; Albe, K.; Latz, A.; et al. Effect of Particle Size and Pressure on the Transport Properties of the Fast Ion Conductor t-Li7SiPS8. *Adv. Energy Mater.* **2023**, *13*, No. 2203873.

(9) Wang, M.; Wolfenstine, J. B.; Sakamoto, J. Temperature dependent flux balance of the $Li/Li_7La_3Zr_2O_{12}$ interface. *Electrochim. Acta* **2019**, *296*, 842−847.

(10) Han, F.; Westover, A. S.; Yue, J.; Fan, X.; Wang, F.; Chi, M.; Leonard, D. N.; Dudney, N. J.; Wang, H.; Wang, C. High electronic conductivity as the origin of lithium dendrite formation within solid electrolytes. *Nature Energy* **2019**, *4*, 187−196.

(11) Zhang, X.; Wang, Q. J.; Harrison, K. L.; Roberts, S. A.; Harris, S. J. Pressure-driven interface evolution in solid-state lithium metal batteries. *Cell Rep. Phys. Sci.* **2020**, *1*, No. 100012.

(12) Lu, P.; Wu, D.; Chen, L.; Li, H.; Wu, F. Air stability of solid-state sulfide batteries and electrolytes. *Electrochem. Energy Revi.* **2022**, *5*, 3.

(13) End, H.; Forster, E.Electrical Contact Resistance: Fundamental Principles. In *Electrical Contacts: Principles and Applications*; CRC Press, 2017; pp 1.

(14) Minafra, N.; Kraft, M. A.; Bernges, T.; Li, C.; Schlem, R.; Morgan, B. J.; Zeier, W. G. Local charge inhomogeneity and lithium distribution in the superionic argyrodites Li6PS5X (X= Cl, Br, I). *Inorg. Chem.* **2020**, *59*, 11009−11019.

(15) Zhang, J.; Lv, J.; Lu, W.; Li, X.; Liu, Y.; Lang, J.; Liu, J.; Wang, Z.; Lu, M.; Sun, H. $Li_{10}GeP_2S_{12}$-based solid electrolyte induced by high pressure for all-solid-state batteries: A facile strategy of low-grain-boundary-resistance. *Chemical Engineering Journal* **2024**, *487*, No. 150452.

(16) Korjus, O.; Mitra, S.; Berrod, Q.; Vanpeene, V.; Appel, M.; Broche, L.; Lyonnard, S.; Villevieille, C. Investigating the densification of Li6PS5Cl solid electrolyte through multi-scale characterization techniques. *Energy Storage Materials* **2025**, *82*, No. 104589.

(17) Sourisseau, C.; Cavagnat, R.; Jobic, S.; Brec, R. Infrared, Raman and resonance Raman spectra and lattice dynamics calculations of the solid potassium (I) palladium (II) thiophosphate compound $KPdPS_4$. *Journal of Raman spectroscopy* **1999**, *30*, 721−731.

(18) Wu, Y.; Bensch, W. Syntheses, structures, and spectroscopic properties of $K_9Nd[PS_4]_4$, $K_3Nd[PS_4]_2$, $Cs_3Nd[PS_4]_2$, and $K_3Nd_3[PS_4]_4$. *Inorganic chemistry* **2008**, *47*, 7523−7534.

(19) Müller, A.; Mohan, N.; Cristophliemk, P.; Tossidis, I.; Dräger, M. Investigation of the vibrational spectra of PS_4^{3-}, CS_3^{2-}, CS_2Se^{2-}, $CSSe_2^{2-}$, CSe_3^{2-}, BCl_2Br and $BClBr_2$. *Spectrochimica Acta Part A: Molecular Spectroscopy* **1973**, *29*, 1345−1356.

(20) Lange, P. L.; Schleid, T. $Li_3La[PS_4]_2$: The First Lithium Lanthanum Ortho-Thiophosphate. *Eur. J. Inorg. Chem.* **2021**, *2021*, 3247−3254.

(21) Sourisseau, C.; Cavagnat, R.; Fouassier, M.; Brec, R.; Elder, S. Infrared, Raman, resonance Raman spectra and lattice dynamics calculations of the solid potassium (I) nickel (II) thiophosphate compound, KNiPS4. *Chemical physics* **1995**, *195*, 351−369.

(22) Naillou, P.; Boulineau, A.; De Vito, E.; Ramos, R.; Azaïs, P. Evidencing Phase Transformations of Li6PS5Cl Argyrodite under Ambient Air and Dry Room Exposure. *ACS Appl. Mater. Interfaces* **2024**, *16*, 53855−53863.

(23) Cao, D.; Zhang, Y.; Nolan, A. M.; Sun, X.; Liu, C.; Sheng, J.; Mo, Y.; Wang, Y.; Zhu, H. Stable thiophosphate-based all-solid-state lithium batteries through conformally interfacial nanocoating. *Nano Lett.* **2020**, *20*, 1483−1490.

(24) Hagen, M.; Schiffels, P.; Hammer, M.; Dörfler, S.; Tübke, J.; Hoffmann, M.; Althues, H.; Kaskel, S. In-situ Raman investigation of polysulfide formation in Li-S cells. *J. Electrochem. Soc.* **2013**, *160*, A1205.

(25) Hassoun, J.; Verrelli, R.; Reale, P.; Panero, S.; Mariotto, G.; Greenbaum, S.; Scrosati, B. A structural, spectroscopic and electrochemical study of a lithium ion conducting $Li_{10}GeP_2S_{12}$ solid electrolyte. *J. Power Sources* **2013**, *229*, 117−122.

(26) Zhang, R.; Wu, Y.; Chen, Z.; Wang, Y.; Zhu, J.; Zhuang, X. The value of in situ/operando Raman spectroscopy in all-solid-state Li batteries. *Journal of Materials Chemistry A* **2023**, *11*, 19195−19209.

(27) Gieck, C. From discrete anions to extended solids: new uranium thiophosphates. Ph.D. thesis, Johannes Gutenberg University Mainz: Mainz, Germany, 2003; Available at https://openscience.ub.uni-mainz.de/server/api/core/bitstreams/47139412-f51a-4497-8094-fb167ab4c044/content.

(28) Sourisseau, C.; Forgerit, J.; Mathey, Y. Vibrational study of the $[P_2S_4^{-6}]$ anion, of some MPS_3 layered compounds (M= Fe, Co, Ni, In_{23}), and of their intercalates with $[Co\ (\eta^5\text{-}C_5H_5)^{+2}]$ cations. *J. Solid State Chem.* **1983**, *49*, 134−149.

(29) Li, X.; Liang, J.; Lu, Y.; Hou, Z.; Cheng, Q.; Zhu, Y.; Qian, Y. Sulfur-rich phosphorus sulfide molecules for use in rechargeable lithium batteries. *Angew. Chem., Int. Ed.* **2017**, *56*, 2937−2941.

(30) Dietrich, C.; Weber, D. A.; Culver, S.; Senyshyn, A.; Sedlmaier, S. J.; Indris, S.; Janek, J.; Zeier, W. G. Synthesis, structural characterization, and lithium ion conductivity of the lithium thiophosphate $Li_2P_2S_6$. *Inorganic chemistry* **2017**, *56*, 6681−6687.

(31) Sang, L.; Haasch, R. T.; Gewirth, A. A.; Nuzzo, R. G. Evolution at the solid electrolyte/gold electrode interface during lithium deposition and stripping. *Chemistry of materials* **2017**, *29*, 3029−3037.

(32) Gabaude, C. M.; Guillot, M.; Gautier, J.-C.; Saudemon, P.; Chulia, D. Effects of true density, compacted mass, compression speed, and punch deformation on the mean yield pressure. *Journal of pharmaceutical sciences* **1999**, *88*, 725−730.

(33) Sun, C.; Grant, D. J. Influence of elastic deformation of particles on Heckel analysis. *Pharm. Dev. Technol.* **2001**, *6*, 193−200.

(34) Patel, S.; Kaushal, A. M.; Bansal, A. K. Effect of particle size and compression force on compaction behavior and derived mathematical parameters of compressibility. *Pharm. Res.* **2007**, *24*, 111−124.
(35) Faka, V.; Agne, M. T.; Lange, M. A.; Daisenberger, D.; Wankmiller, B.; Schwarzmüller, S.; Huppertz, H.; Maus, O.; Helm, B.; Böger, T.; et al. Pressure-induced dislocations and their influence on ionic transport in Li+-conducting argyrodites. *J. Am. Chem. Soc.* **2024**, *146*, 1710−1721.
(36) Vadhva, P.; Hu, J.; Johnson, M. J.; Stocker, R.; Braglia, M.; Brett, D. J.; Rettie, A. J. Electrochemical impedance spectroscopy for all-solid-state batteries: theory, methods and future outlook. *ChemElectroChem.* **2021**, *8*, 1930−1947.
(37) Shao, B.; Huang, Y.; Han, F. Electronic conductivity of lithium solid electrolytes. *Adv. Energy Mater.* **2023**, *13*, No. 2204098.
(38) Reddy, M. V.; Julien, C. M.; Mauger, A.; Zaghib, K. Sulfide and oxide inorganic solid electrolytes for all-solid-state Li batteries: a review. *Nanomaterials* **2020**, *10*, 1606.
(39) Aoun, S. B.; Bouklah, M.; Khaled, K.; Hammouti, B. Electrochemical impedance spectroscopy investigations of steel corrosion in acid media in the presence of thiophene derivatives. *Int. J. Electrochem. Sci.* **2016**, *11*, 7343−7358.
(40) Karlsson, C.; Drüschler, M.; Huber, B.; Wallauer, J.; Klemm, C. P.; Kranz, S.; Schöll, M. *Application Note: Three-Electrode All-Solid-State Battery Cycling*. rhd instruments GmbH & Co. KG, 2023, Available at https://docs.rhd-instruments.de/appnotes/application-note_Three-Electrode_ASSB.pdf.
(41) Drüschler, M.; Huber, B.; Wallauer, J.; Klemm, C. P.; Kranz, S.; Schöll, M.; Karlsson, C. *Introduction to Applied Electrochemical Impedance Spectroscopy*. rhd instruments GmbH & Co. KG, 2023.
(42) McAdams, E.; Lackermeier, A.; McLaughlin, J.; Macken, D.; Jossinet, J. The linear and non-linear electrical properties of the electrode-electrolyte interface. *Biosens. Bioelectron.* **1995**, *10*, 67−74.
(43) Fontanella, J. Pressure and temperature variation of the electrical conductivity of poly (propylene glycol) containing $LiCF_3SO_3$. *J. Chem. Phys.* **1999**, *111*, 7103−7109.
(44) Fu, Z.-H.; Chen, X.; Zhao, C.-Z.; Yuan, H.; Zhang, R.; Shen, X.; Ma, X.-X.; Lu, Y.; Liu, Q.-B.; Fan, L.-Z.; et al. Stress regulation on atomic bonding and ionic diffusivity: mechanochemical effects in sulfide solid electrolytes. *Energy Fuels* **2021**, *35*, 10210−10218.
(45) Faka, V.; Agne, M. T.; Till, P.; Bernges, T.; Sadowski, M.; Gautam, A.; Albe, K.; Zeier, W. G. Pressure dependence of ionic conductivity in site disordered lithium superionic argyrodite Li 6 PS 5 Br. *Energy Advances* **2023**, *2*, 1915−1925.
(46) Yang, H.; Wu, N. Ionic conductivity and ion transport mechanisms of solid-state lithium-ion battery electrolytes: A review. *Energy Science & Engineering* **2022**, *10*, 1643−1671.
(47) Ma, C.; Chen, K.; Liang, C.; Nan, C.-W.; Ishikawa, R.; More, K.; Chi, M. Atomic-scale origin of the large grain-boundary resistance in perovskite Li-ion-conducting solid electrolytes. *Energy Environ. Sci.* **2014**, *7*, 1638−1642.
(48) Dawson, J. A.; Canepa, P.; Famprikis, T.; Masquelier, C.; Islam, M. S. Atomic-scale influence of grain boundaries on Li-ion conduction in solid electrolytes for all-solid-state batteries. *J. Am. Chem. Soc.* **2018**, *140*, 362−368.
(49) Wiers, B. M.; Foo, M.-L.; Balsara, N. P.; Long, J. R. A solid lithium electrolyte via addition of lithium isopropoxide to a metal−organic framework with open metal sites. *J. Am. Chem. Soc.* **2011**, *133*, 14522−14525.
(50) Kuzmin, A.; Plekhanov; Lesnichyova, A. Influence of impurities on the bulk and grain-boundary conductivity of $CaZrO_3$-based proton-conducting electrolyte: a distribution of relaxation time study. *Electrochim. Acta* **2020**, *348*, No. 136327.
(51) Yamakov, V. I.; Rains, A. A.; Kang, J. H.; Das, L.; Rashid, R.; Su, J.; Viggiano, R. P.; Connell, J. W.; Lin, Y. Pressure Dependence of Solid Electrolyte Ionic Conductivity: A Particle Dynamics Study. *ACS Appl. Mater. Interfaces* **2023**, *15*, 27243−27252.
(52) Doux, J.-M.; Yang, Y.; Tan, D. H.; Nguyen, H.; Wu, E. A.; Wang, X.; Banerjee, A.; Meng, Y. S. Pressure effects on sulfide electrolytes for all solid-state batteries. *Journal of Materials Chemistry A* **2020**, *8*, 5049−5055.
(53) Bachman, J. C.; Muy, S.; Grimaud, A.; Chang, H.-H.; Pour, N.; Lux, S. F.; Paschos, O.; Maglia, F.; Lupart, S.; Lamp, P.; et al. Inorganic solid-state electrolytes for lithium batteries: mechanisms and properties governing ion conduction. *Chem. Rev.* **2016**, *116*, 140−162.
(54) Rao, R. P.; Adams, S. Studies of lithium argyrodite solid electrolytes for all-solid-state batteries. *physica status solidi (a)* **2011**, *208*, 1804−1807.
(55) Muruganantham, R.; Wu, H.-W.; Lo, Y.; Liu, W.-R. Improving electrochemical stability by modifying the Li6PS5Cl entailed with the mixed phase of $Li_{6.4}La_3Zr_{1.4}Ta_{0.6}O_{12}$ composite solid electrolytes for all-solid-state lithium battery applications. *Surf. Coat. Technol.* **2024**, *479*, No. 130480.
(56) Chen, J.; Fang, M.; Wu, Q.; Tang, S.; Zheng, J.; Wei, C.; Cao, X.; Shi, Y.; Xu, N.; He, Y. Insights into the Atomic Mechanism of Lithium-Ion Diffusion in Li6PS5Cl via a Machine Learning Potential. *Chem. Mater.* **2025**, *37*, 591−599.
(57) Kim, T.; Hood, Z. D.; Sundar, A.; Mane, A. U.; Lagunas, F.; Kumar, K.; Sunariwal, N.; Cabana, J.; Tepavcevic, S.; Elam, J. W.; et al. Suppressing Atmospheric Degradation of Sulfide-Based Solid Electrolytes via Ultrathin Metal Oxide Layers. *ACS Materials Letters* **2024**, *6*, 5409−5417.
(58) Maia, B. A.; Gomes, B. M.; Guerreiro, A. N.; Santos, R. M.; Braga, M. H. Cathodes pinpoints for the next generation of energy storage devices: the LiFePO4 case study. *Journal of Physics: Materials* **2024**, *7*, No. 025001.
(59) Gorai, P.; Famprikis, T.; Singh, B.; Stevanovic, V.; Canepa, P. Devil is in the defects: electronic conductivity in solid electrolytes. *Chem. Mater.* **2021**, *33*, 7484−7498.
(60) Kraft, M. A.; Culver, S. P.; Calderon, M.; Böcher, F.; Krauskopf, T.; Senyshyn, A.; Dietrich, C.; Zevalkink, A.; Janek, J.; Zeier, W. G. Influence of lattice polarizability on the ionic conductivity in the lithium superionic argyrodites Li_6PS_5X (X= Cl, Br, I). *J. Am. Chem. Soc.* **2017**, *139*, 10909−10918.
(61) Gautam, A.; Sadowski, M.; Prinz, N.; Eickhoff, H.; Minafra, N.; Ghidiu, M.; Culver, S. P.; Albe, K.; Fässler, T. F.; Zobel, M.; et al. Rapid crystallization and kinetic freezing of site-disorder in the lithium superionic argyrodite Li_6PS_5Br. *Chem. Mater.* **2019**, *31*, 10178−10185.
(62) Hanghofer, I.; Brinek, M.; Eisbacher, S.; Bitschnau, B.; Volck, M.; Hennige, V.; Hanzu, I.; Rettenwander, D.; Wilkening, H. Substitutional disorder: structure and ion dynamics of the argyrodites Li_6PS_5Cl, Li_6PS_5Br and Li_6PS_5I. *Phys. Chem. Chem. Phys.* **2019**, *21*, 8489−8507.
(63) Kim, T.; Kim, K.; Lee, S.; Song, G.; Jung, M. S.; Lee, K. T. Thermal runaway behavior of Li6PS5Cl solid electrolytes for $LiNi_{0.8}Co_{0.1}Mn_{0.1}O_2$ and $LiFePO_4$ in all-solid-state batteries. *Chem. Mater.* **2022**, *34*, 9159−9171.
(64) Kim, K. T.; Woo, J.; Kim, Y.-S.; Sung, S.; Park, C.; Lee, C.; Park, Y. J.; Lee, H.-W.; Park, K.; Jung, Y. S. Ultrathin Super-hydrophobic Coatings for Air-Stable Inorganic Solid Electrolytes: Toward Dry Room Application for All-Solid-State Batteries. *Adv. Energy Mater.* **2023**, *13*, No. 2301600.
(65) Yu, C.; van Eijck, L.; Ganapathy, S.; Wagemaker, M. Synthesis, structure and electrochemical performance of the argyrodite Li6PS5Cl solid electrolyte for Li-ion solid state batteries. *Electrochim. Acta* **2016**, *215*, 93−99.
(66) Letoullec, R.; Pinceaux, J.; Loubeyre, P. The membrane diamond anvil cell. *High Pressure Science and Technology* **1990**, *5*, 871−873.
(67) Dewaele, A.; Torrent, M.; Loubeyre, P.; Mezouar, M. Compression curves of transition metals in the Mbar range: Experiments and projector augmented-wave calculations. *Physi. Rev. B Condens. Matter Mater. Phys.* **2008**, *78*, No. 104102.
(68) Pacetti, S.; Karlsson, C. *Application Note: Distinguishing Bulk and Grain Boundary Conductivity in Solid Electrolytes*. rhd instruments GmbH & Co. KG, 2024; Available at https://docs.rhd-instruments.

https://doi.org/10.1021/acs.jpcc.5c06227
J. Phys. Chem. C 2026, 130, 3040−3049

de/appnotes/application-note_Bulk_vs_Grain_Boundary_Conductivity.pdf.

https://doi.org/10.1021/acs.jpcc.5c06227
J. Phys. Chem. C 2026, 130, 3040−3049